Solar Phys (2019) 294:54
https://doi.org/10.1007/s11207-019-1443-5

Interplanetary Coronal Mass Ejections During Solar Cycles 23 and 24: Sun–Earth Propagation Characteristics and Consequences at the Near-Earth Region

M. Syed Ibrahim[1] · Bhuwan Joshi[1] · K.-S. Cho[2,3] · R.-S. Kim[2,3] · Y.-J. Moon[4]

Received: 10 September 2018 / Accepted: 11 April 2019
© Springer Nature B.V. 2019

Abstract In this article, we present a statistical study probing the relation between interplanetary coronal mass ejections (ICMEs) observed at 1 AU and their corresponding coronal mass ejections at the near-Sun region. The work encompasses the ICME activity that occurred during Solar Cycles 23 and 24 (1996 – 2017) while presenting an overall picture of ICME events during the complete Solar Cycle 24 for the first time. The importance of this study further lies in comparing two subsets of ICMEs, *i.e.* magnetic clouds (MCs) and ejecta (EJ), to explore how the observed structures of ICMEs at 1 AU could be associated with the properties of CMEs during their launch at the Sun. We find that, although Solar Cycle 24 saw a significant reduction in the number of ICME events compared to the previous cycle, the fraction of MCs was much higher during Cycle 24 than Cycle 23 (60% *versus* 41%). In general, the ICME transit-time decreases with the increase in the CME initial speed, although a broad range of transit times were observed for a given CME speed. We also find that the high-speed ICMEs ($\gtrsim 500$ km s^{-1}) form a distinct group in terms of the deficit in their transit times when compared with low-speed events ($\lesssim 500$ km s^{-1}), which means that high-speed ICMEs acquire a much higher internal energy from the source active regions during the initiation process that effectively overcomes the aerodynamic drag force while they transit in the interplanetary medium. The CME propagation from the Sun to the near-Earth environment shows both an overall positive and negative acceleration (*i.e.* deceleration), although the acceleration is limited to only low-speed CMEs that are launched with a speed comparable with or less than the mean solar wind speed ($\approx 400 - 450$ km s^{-1}). Within a given cycle, the similarities of MC and EJ profiles with respect to the CME–ICME speed relation as well as interplanetary acceleration support the hypothesis that all CMEs

✉ M. Syed Ibrahim
syed@prl.res.in

1 Physical Research Laboratory, Udaipur Solar Observatory, Udaipur 313001, India

2 Korea Astronomy and Space Science Institute, Daejeon 305-348, South Korea

3 Department of Astronomy and Space Science, University of Science and Technology, Daejeon, South Korea

4 School of Space Research, Kyung Hee University, Yongin, Gyeonggi-Do, 446-701, South Korea

Published online: 03 May 2019

have a flux rope structure and that the trajectory of the CMEs essentially determines the observed ICME structure at 1 AU.

Keywords Coronal mass ejections · Interplanetary coronal mass ejections · Magnetic clouds · Ejecta

1. Introduction

Coronal mass ejections (CMEs) and associated eruptive flares are the most violent manifestations of the active Sun. While a flare is attributed to the sudden and impulsive release of a huge amount of energy ($\approx 10^{27} - 10^{32}$ ergs on the time scales of a few to several tens of minutes) from a localized region of the solar atmosphere, CMEs primarily represent the eruption of a large amount of plasma from the Sun ($\approx 10^{14} - 10^{16}$ g with speeds ranging from < 100 to $\gtrsim 2500$ km s^{-1}). During a CME, the large-scale eruption of plasma and magnetic field produces significant changes in the magnetic configuration of the solar corona (see the reviews by Webb and Howard, 2012; Schmieder, Aulanier, and Vršnak, 2015; Chen, 2017). Interplanetary CMEs (or ICMEs) are known to drive severe space weather events. Earth-directed CMEs (known as halo CMEs) can generate non-recurrent geomagnetic storms when colliding with Earth's magnetic field, provided that they contain a strong and sustained southward magnetic field component (see the review by Zurbuchen and Richardson, 2006).

Early observations of the solar wind confirm that CMEs at 1 AU generally have distinct plasma and field signatures by which can be distinguished from the ordinary solar wind (see the review by Gosling, 1990). The characteristic features of ICMEs in the flow of the solar wind include abnormally low proton and electron temperatures, and bidirectional suprathermal electron strahls along with anomalies in plasma composition (Cane and Richardson, 2003; Richardson and Cane, 2004). With the availability of continuous *in situ* observations at 1 AU of multiple plasma and magnetic field parameters of the solar wind, it has become possible to identify the arrival of Earth-directed ICMEs corresponding to CMEs launched from the Sun several hours earlier. There has been a continued interest in assessing the relation among kinematical properties of CMEs at the near-Sun region, their propagation characteristics through the interplanetary medium, and the physical properties of corresponding ICMEs at the near-Earth environment.

Burlaga *et al.* (1981) identified a subset of ICMEs showing a characteristic pattern in which their passage is accompanied by the enhancement of the magnetic field (> 10 nT) that rotates slowly through a large angle (Klein and Burlaga, 1982). Such structures are termed magnetic clouds (MCs). The modeling of the magnetic field configuration of MCs suggests these structures to be associated with a magnetic flux rope. Notably the flux rope interpretation is also consistent with the occasional detection of the helical structure of the CME in the corona and near-Sun region (Dere *et al.*, 1999; Xie, Gopalswamy, and St. Cyr, 2013; Cho *et al.*, 2013). We also note that typical features of an MC can also be completely absent or only partially present in several ICMEs (Burlaga *et al.*, 2001), which points toward the complexity associated with the structural evolution of the CMEs. When MC features are absent, the ICMEs are referred to as ejecta (EJ). For a proper understanding of the interplanetary consequences of CMEs, it is therefore very important to identify the different structures associated with ICMEs (*i.e.* MCs and EJ) and their associations with their corresponding near-Sun counterparts.

The motivation of the present article is to study the association between ICMEs at 1 AU and CMEs at the near-Sun region during Solar Cycles 23 and 24. We particularly focus

on the propagation characteristics of the ICMEs, *i.e.* transit time and IP acceleration, and their variations along different solar cycles. We further divide ICMEs into two subsets – MCs and EJ, to explore how the observed ICME structures at 1 AU could be associated with the corresponding CME properties during the early evolution at the near-Sun region. In Section 2, we provide information as regards the sources of the observational data. We analyze the data and explain the results in detail in Section 3. The main conclusions of the study are given in Section 4.

2. Data and Selection Criterion

Our study is based on data from the following catalogs.

1. *Solar and Heliospheric Observatory* (SOHO) *Large Angle and Spectroscopic Coronagraph* (LASCO) CME catalog[1]: This catalog is used to study the properties of CMEs at the near-Sun region that have an ICME counterpart at 1 AU. The catalog is generated and maintained at the Coordinated Data Analysis Workshop (CDAW) Data Center by NASA and The Catholic University of America in cooperation with the Naval Research Laboratory. The catalog was used to study some of the initial parameters of the CME corresponding to ICMEs at the near-Sun region, *viz.* onset time and initial speed (*i.e.* the linear speed within LASCO field of view).
2. Near-Earth ICME catalog[2]: The present analysis is primarily based on the catalog compiled by Ian Richardson and Hilary Cane and contains a list of ICMEs detected by *in situ* probes from May 1996 to September 2017 (Cane and Richardson, 2003). The catalog provides several useful parameters of the ICMEs, out of which the parameters of interest are the estimated start and end times of the ICME, the mean ICME speed, the minimum value of the geomagnetic Dst index during the period between the disturbance and the ICME trailing edge, and the time of CME onset in the solar corona, based on LASCO observations, which is probably associated with the ICME in question. Notably, the catalog also marks those ICME events for which an associated CME at the near-Sun region has been identified in LASCO observations. The criteria used for the identification of the CME–ICME association have been described in Cane and Richardson (2003). The onset time of the corresponding CME (*i.e.* the time of the first CME observations by LASCO) is listed in the catalog and this information forms the basis for the calculation of the CME transit-time from the near-Sun to the near-Earth environment. Obviously, the analyses have considered only those ICME events for which the CME–ICME association is confirmed in the catalog. A very useful piece of information included in the catalog is whether the observed ICME presents a magnetic cloud (MC) structure or not, based on the criteria proposed by Burlaga *et al.* (1981). When an ICME lacks most of the typical features of a magnetic cloud, it is called ejecta (EJ). Kim *et al.* (2013) have used the same terminology for defining two distinct classes of ICMEs *i.e.* MC and EJ (see also Burlaga, 2001). The catalog also marks complex events where the MC structures cannot be fully defined.

In this study, we consider all ICMEs divided in two subsets, *i.e.* MCs or EJ. Examples of MC and EJ type ICMEs along with their corresponding CMEs are shown in Figures 1 and 2, respectively. In this analysis, we do not study complex cases explicitly although these are included in our master list of all ICMEs.

[1] https://cdaw.gsfc.nasa.gov/CME_list/.

[2] http://www.srl.caltech.edu/ACE/ASC/DATA/level3/icmetable2.htm.

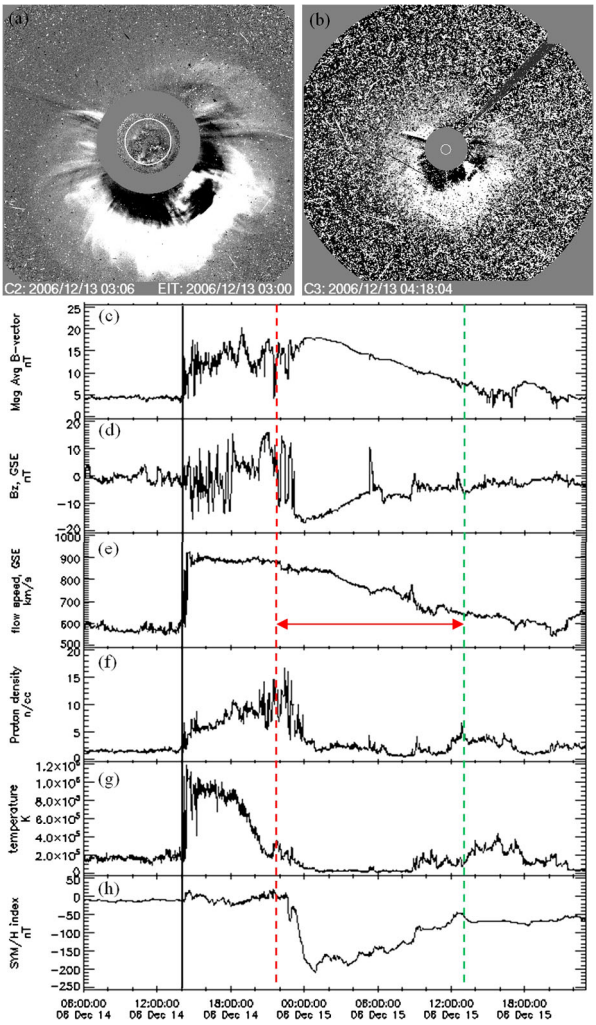

Figure 1 An example of a CME that exhibited an MC type ICME structure at 1 AU. (**a**) and (**b**) present LASCO C2 and C3 observations, respectively, of the CME on 13 December 2006. Panels (**c**) – (**h**) show *in situ* measurements of various ICME associated parameters at 1 AU, *viz.* total magnetic field strength, the z-component of the magnetic field, flow speed, proton density, proton temperature, SYM-H index (*i.e.* high resolution Dst index). The *vertical black line* indicates the arrival of an IP shock. *Red* and *green dotted lines* mark start and end times, respectively, of the ICME.

3. Analysis and Results

3.1. Statistical Variations of CME–ICME Events

Table 1 provides statistics of the occurrence of ICMEs along with the three subsets (*i.e.* MCs, EJ, and complex events) during Solar Cycles 23 and 24. We note a drastic reduction in the number of ICMEs during Cycle 24 compared with the previous one (151 *versus* 62). Interestingly, with respect to the total ICMEs, the fraction of MC-type events is much larger during Cycle 24 (60%) than during Cycle 23 (41%). Obviously, Solar Cycle 24 presents a much lower percentage of the EJ and complex cases compared with the previous cycle.

In Figure 3, we plot histograms of the initial speed of CMEs and corresponding speed of the ICMEs for Solar Cycles 23 and 24. The comparison of near-Sun CME observations (Figures 3a and b) indicates that CMEs exhibited a wide range of initial speeds for both cycles; however, Cycle 24 had fewer high-speed CMEs than Cycle 23. On the other hand,

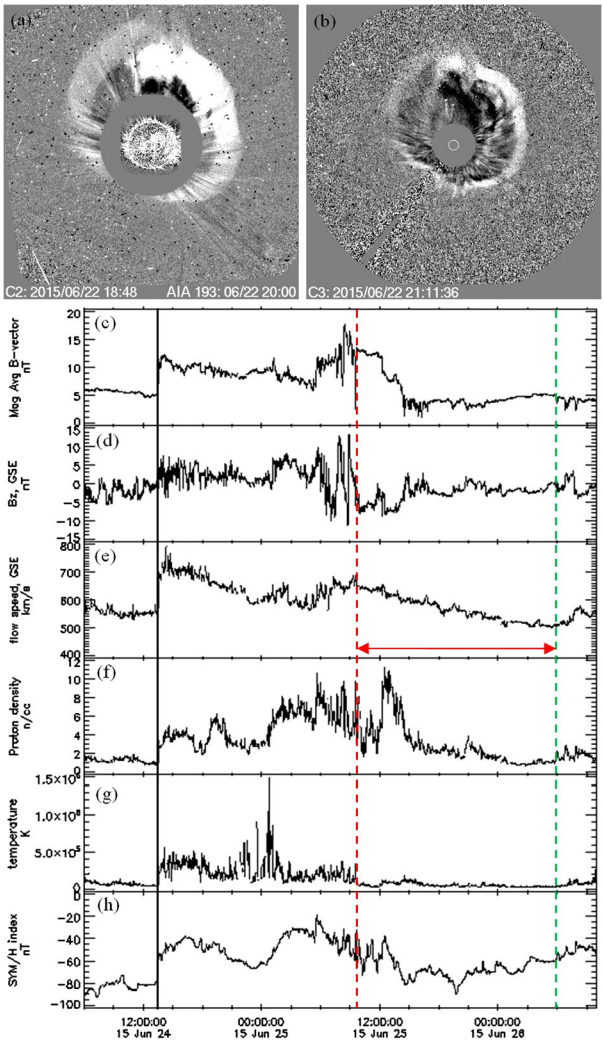

Figure 2 Same as in Figure 1, but for the CME that exhibited an EJ-type structure at 1 AU. The images shown in (**a**) and (**b**) correspond to 22 June 2015.

Table 1 Occurrence of ICMEs during Solar Cycles 23 and 24 for all kinds of events, magnetic clouds (MC), ejecta (EJ), and complex events.

Solar cycle	Number of events			
	Total	MC	EJ	Complex
23	149	62 (41%)	44 (30%)	43 (29%)
24	62	37 (60%)	9 (15%)	16 (25%)

the ICME speed range is very narrow (Figures 3c and d) and tends to a distribution around the ambient solar wind speed ($\approx 400-450\ \mathrm{km\,s^{-1}}$).

To show how the CMEs, included in the database, evolve at the near-Sun region, we plot the histogram of CME width in Figures 4a and b. We find that most ICME–CME associations correspond to wide CMEs with angular extents $\geq 100°$. We would like to mention that the initial CME speeds (see Figure 3), analyzed in this work in the context of Sun–

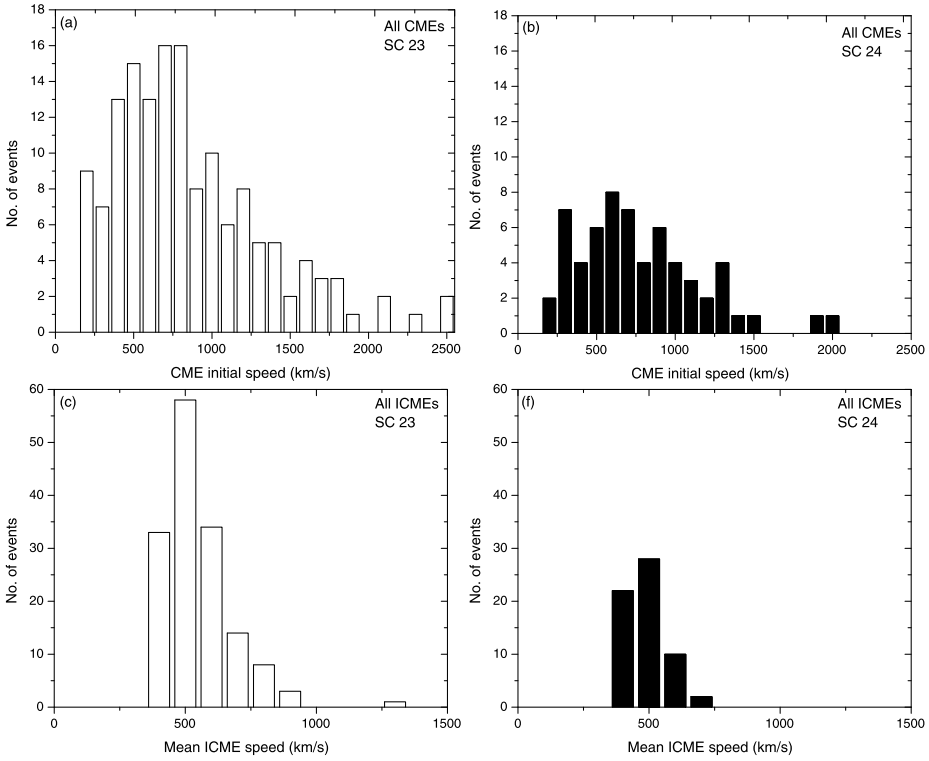

Figure 3 *Top panels*: histograms of the initial speeds of CMEs in the LASCO field of view for Solar Cycles 23 (**a**) and 24 (**b**). *Bottom panels*: histograms of ICME speeds at 1 AU for Solar Cycles 23 (**c**) and 24 (**d**).

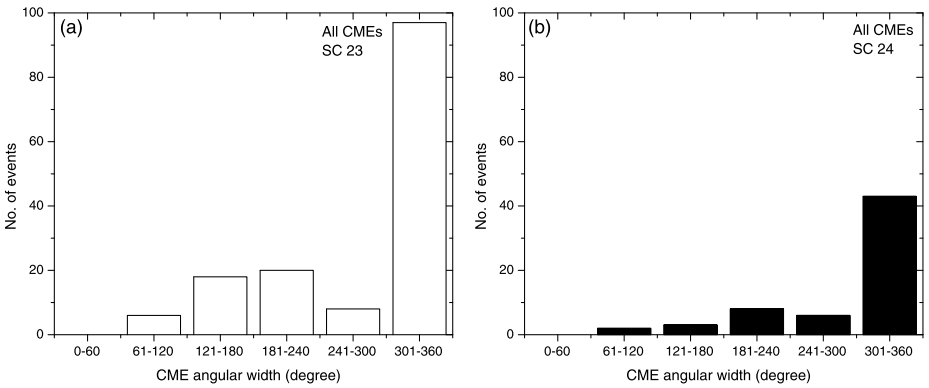

Figure 4 Histograms of CME widths for Solar Cycles 23 (**a**) and 24 (**b**). Note that the CMEs selected for the histograms are those events for which CME–ICME associations have been clearly identified.

Earth propagation properties of ICMEs along with their characteristics at 1 AU, are directly obtained from LASCO observations. The coronagraphic observations of CMEs (especially halo CMEs) are subject to a projection effect which is a limitation as regards determining

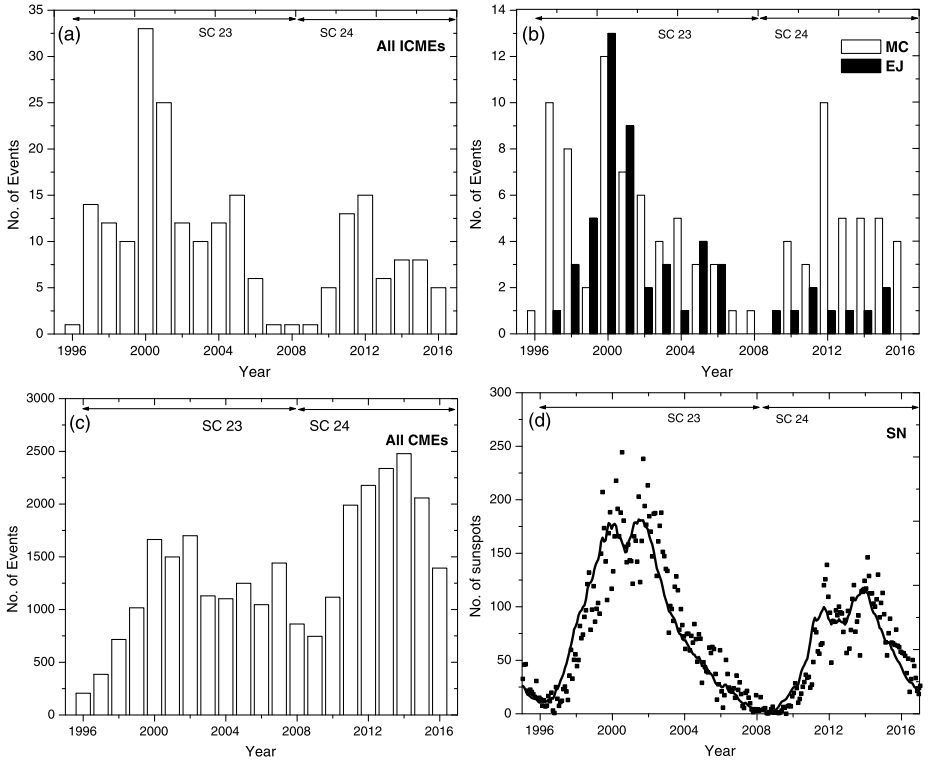

Figure 5 (**a**): Histograms showing the annual occurrence of ICMEs during Solar Cycles 23 and 24. (**b**): Two types of ICMEs, *i.e.* MCs (*white bar*) and EJs (*black bar*), are shown separately for Solar Cycles 23 and 24. We find that, in comparison with Cycle 23, Cycle 24 is much poorer in producing ICMEs. In particular, we note a drastic reduction in EJ type events during Cycle 24. (**c**): For a comparison between occurrence rate of ICMEs reaching the near-Earth region with the total number of CMEs launched at the Sun, we draw a histogram of annual counts of CMEs. Inspection of histograms (**a**) and (**c**) reveals that ICMEs that reach the near-Earth region form a very small fraction of the total CMEs originating from the Sun. For example, we find annual rates of ICMEs and CMEs to be about 11 events year^{-1} and 1397 events year^{-1}, respectively. (**d**): To show the evolution of CME and IMCE activity with the solar cycle, we plot monthly sunspot numbers (SN). The *solid line* indicates 11 points running average.

the true radial velocity and width of CMEs. In this study, however, we simply use the linear speed of CMEs, without accounting for projection effects.

In Figure 5, we show a histogram of the total ICMEs (panel a) along with MC and EJ events (panel b) during Solar Cycles 23 and 24. For comparison, the histogram of the total annual CME counts and the plot of the monthly sunspot number during the same period are also shown in Figure 5c and d, respectively. We note that although Cycle 24 is significantly weaker than the previous cycle in terms of sunspot numbers, it showed a higher CME activity. We find that the years 2000 and 2012 had the maximum number of ICMEs during Cycles 23 and 24, respectively (Figure 5a). The bar chart of MC and EJ events shows some very interesting variations in their temporal evolution with the different phases of the solar cycles. We find a dominance of MCs during the rise phase of the solar cycle, while EJs took over the yearly count when the cycle was in its maximum phase. During Cycle 24, we find a dominance of MCs all along.

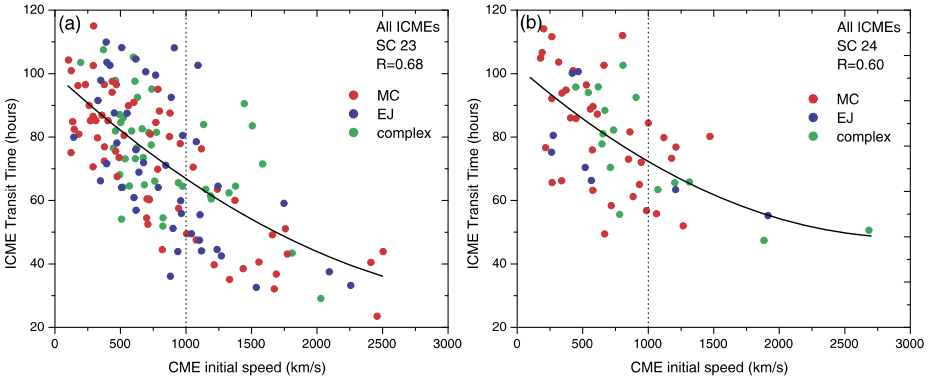

Figure 6 Relationships between the initial CME speeds and the observed ICME transit-times for Solar Cycles 23 (**a**) and 24 (**b**). The *black curves* indicate the quadratic least-squares fit to the ICME transit-times ($T_{\rm ICME}$) and the initial CME speeds ($V_{\rm CME}$) (see Equations 1 and 2 for Cycles 23 and 24, respectively). The correlation coefficient (R) for the quadratic fitting is annotated at the top right corner of each panel. *Dotted vertical lines* are plotted at $V_{\rm CME} = 1000$ km s^{-1} to visualize the distribution of high- and low-speed CMEs. We note that the number of high-speed CMEs ($V \gtrsim 1000$ km s^{-1}) in Cycle 24 is much smaller (14) than in the previous cycle (44).

It is worth noting that the annual rate of CMEs that arrive at the near-Earth region (*i.e.* the ICMEs presented in Figure 5a) is about 11 events year^{-1}, which forms a very small fraction of the total CMEs originating from the Sun (*cf.* Figure 5a and c). For example, considering all the CMEs observed by LASCO in the same period, the annual CME rate is 1397 events year^{-1}.

3.2. CME Transit Time from the Sun to 1 AU

The transit time of an ICME ($T_{\rm ICME}$) is estimated from the difference between the CME onset time in the LASCO C2 field of view and the arrival of the ICME to the near-Earth region. In Figure 6, we plot the transit time for all ICMEs as a function of the initial speed of the corresponding CME for Solar Cycles 23 (panel (a)) and 24 (panel (b)). For a clearer presentation, data points corresponding to MCs, EJ, and complex cases are denoted by red, blue, and green colors, respectively. For Solar Cycle 23, the transit time ranges between $\approx$120 and 30 hours, while for Solar Cycle 24 the lower limit for the transit time is at a significantly higher level, $\approx$45 hours. Obviously, the fewer high-speed CME events during Solar Cycle 24 would correspond to the majority of ICMEs showing larger Sun–Earth transit times. The least-square fittings to a second order polynomial to ICME transit-time *versus* initial CME speed for Cycles 23 and 24 are given by the following equations, respectively:

$$T_{\rm ICME} = 99.9 - 0.04 V_{\rm CME} + 5.0 \times 10^{-6} {V_{\rm CME}}^2, \quad (1)$$

$$T_{\rm ICME} = 102.3 - 0.04 V_{\rm CME} + 6.0 \times 10^{-6} {V_{\rm CME}}^2. \quad (2)$$

In Figure 7, we show the deviations (in %) of the observed ICME transit-time from the empirical relations (given by Equations 1 and 2) for Solar Cycles 23 (panel a) and 24 (panel b).

In Figure 8, we provide the relation between ICME transit-times and CME initial speeds separately for MC and EJ types for Solar Cycles 23 and 24. We find that Solar Cycle 23, in

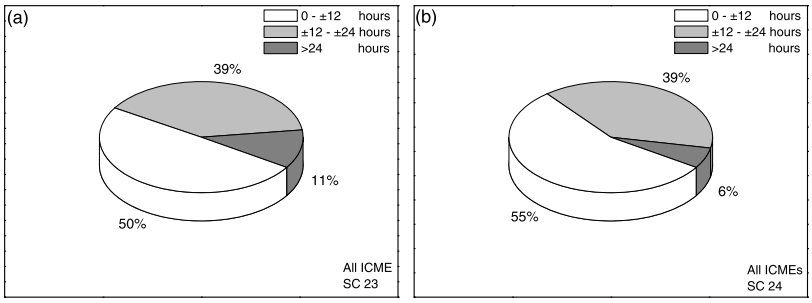

Figure 7 Pie chart of the deviations of the observed ICME transit-times from the average fitted transit times for Solar Cycles 23 (**a**) and 24 (**b**).

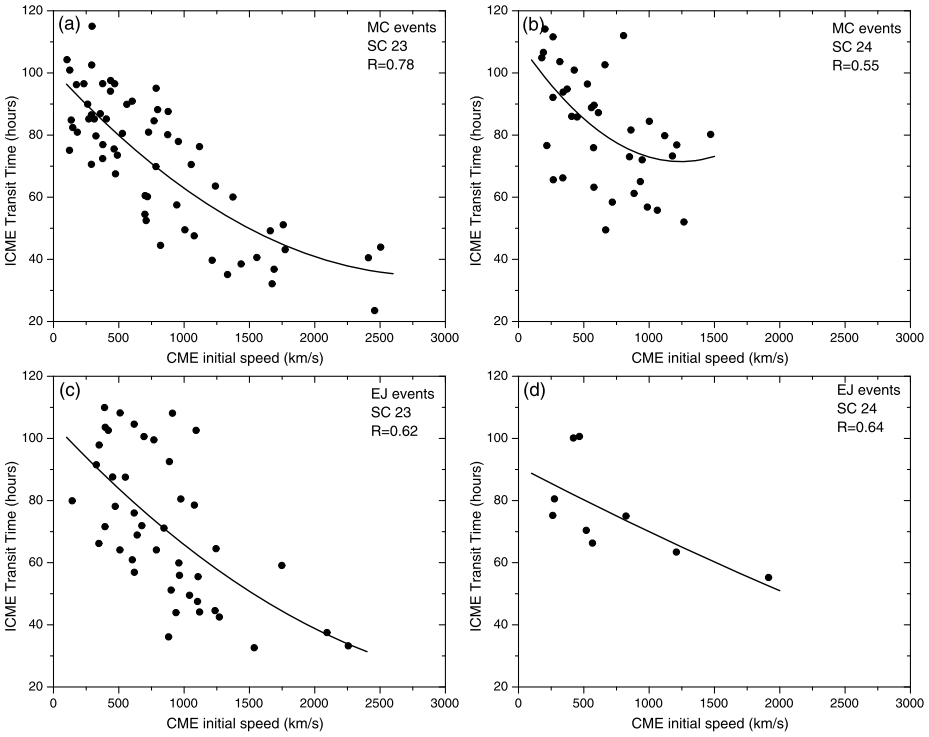

Figure 8 Relations between the initial CME speeds and the observed ICME transit-times separately for MC (*top panels*) and EJ (*bottom panels*) type ICMEs for Solar Cycles 23 (left panels) and 24 (*right panels*). The *black curves* indicate the quadratic least-squares fit to the ICME transit-time for MC and EJ cases (*i.e.* $T_{\rm MC}$ and $T_{\rm EJ}$) and the computed initial CME speeds ($V_{\rm CME}$) (see Equations 3 – 6). The correlation coefficient (R) for the quadratic fitting is indicated at the *top right corner of each panel*.

comparison with the next cycle, presents a more systematic pattern in terms of variations of CME initial speeds with ICME transit-times. During Cycle 24, we do not find any MC with speed > 1500 km s^{-1}, while there are several very high-speed MCs during Cycle 23 within the speed range of $\approx 1500-2500$ km s^{-1}. Due to the occurrence of very high-speed MC events, Cycle 23 exhibited lower transit times (Figure 8a). We further notice a very small

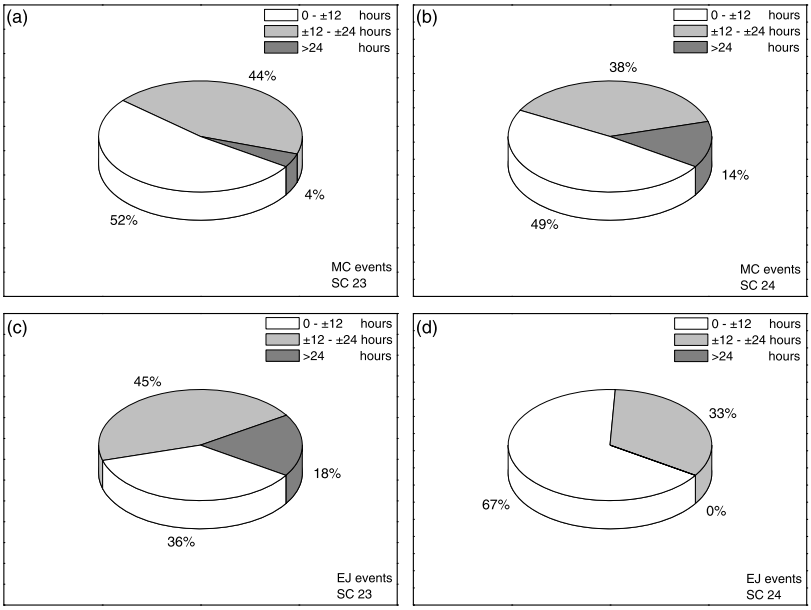

Figure 9 Pie chart of the deviations of the observed ICME transit-times from the average fitted transit time separately for MC (*top panels*) and EJ (*bottom panels*) type ICMEs for Solar Cycles 23 (*left panels*) and 24 (*right panels*).

number of EJ during Cycle 24 (Table 1 and Figure 8(d)). The best fittings to a second order polynomial to MC transit times *versus* initial speeds of CMEs for Cycles 23 and 24 give us an idea about the average pattern of MC propagation and are given by Equations 3 and 4, respectively:

$$T_{\mathrm{MC}} = 100.9 - 0.05 V_{\mathrm{CME}} + 8.0 \times 10^{-6} {V_{\mathrm{CME}}}^2, \tag{3}$$

$$T_{\mathrm{MC}} = 110.2 - 0.06 V_{\mathrm{CME}} + 2.5 \times 10^{-6} {V_{\mathrm{CME}}}^2. \tag{4}$$

For EJ events, the relationships between transit times *versus* initial speeds of CMEs for Cycles 23 and 24 are given by Equations 5 and 6, respectively:

$$T_{\mathrm{EJ}} = 104.8 - 0.05 V_{\mathrm{CME}} + 6.0 \times 10^{-6} {V_{\mathrm{CME}}}^2, \tag{5}$$

$$T_{\mathrm{EJ}} = 90.9 - 0.02 V_{\mathrm{CME}} + 1.0 \times 10^{-6} {V_{\mathrm{CME}}}^2. \tag{6}$$

We note that Equation 6 may not yield a very reliable statistical relation between the ICME transit-times and CME initial speeds because of a very limited number of data points. Figure 9 shows the deviations (in %) of the observed transit times of MCs and EJs from the empirical relations given by Equations 3 – 6 for Cycles 23 and 24.

3.3. ICME Speeds at 1 AU

In Figure 10, we plot the ICME speeds at 1 AU as a function of ICME transit-times from the Sun to the near-Earth environment. The dashed curve in each panel represents the estimated travel time assuming that all the CMEs propagate between the Sun–Earth distance with a

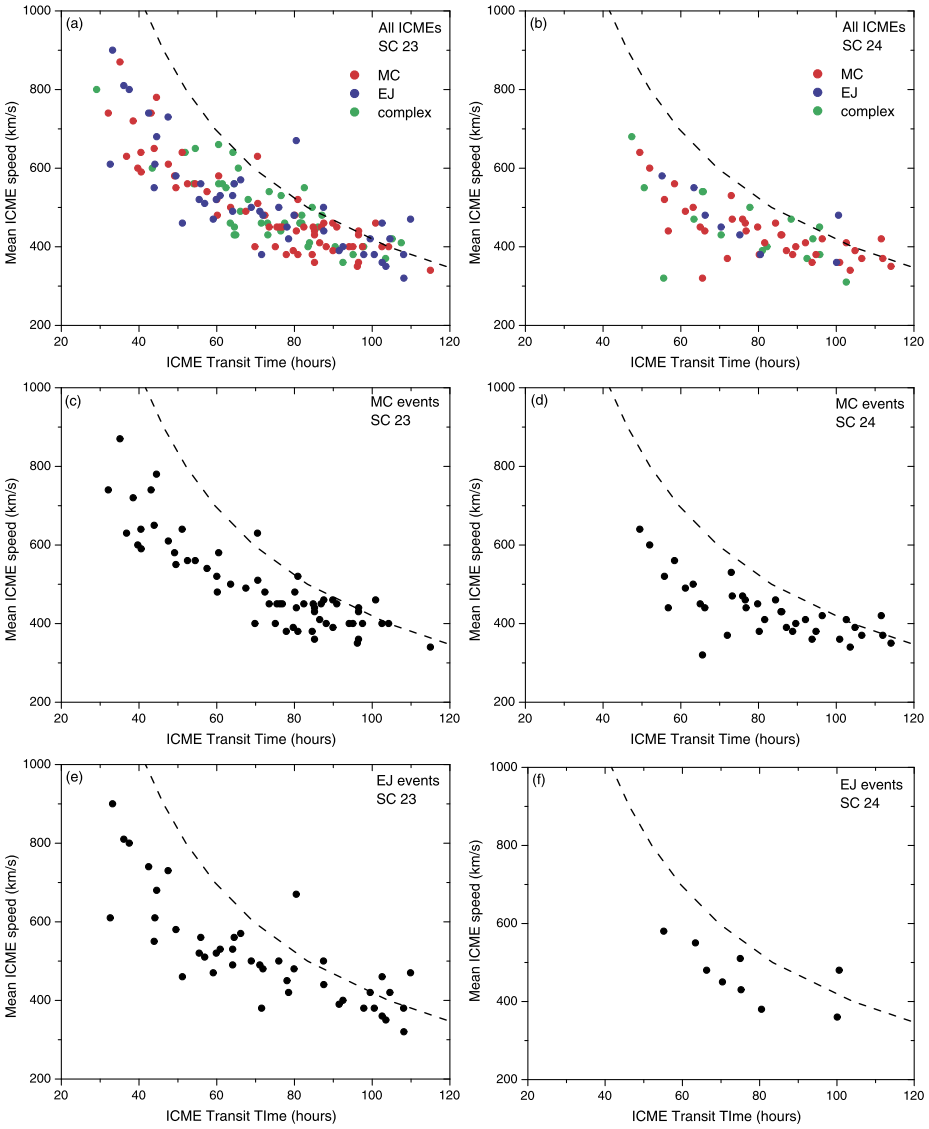

Figure 10 Relations between the mean ICME speeds and the observed ICME transit-times for all ICMEs (*top panels*), MC (*middle panels*), and EJ type events (*bottom panels*) for Solar Cycles 23 (*left panels*) and 24 (*right panels*). *Dashed curves* show the estimated travel time assuming that CMEs propagated with a constant speed which is equal to their speed at 1 AU (*i.e.* mean ICME speed). We note that most of the events lie below the hypothetical constant speed curve. Further, the transit times for fast ICMEs ($\gtrsim 500$ km s^{-1}) are distinctly shorter than those expected from their observed speeds at 1 AU which can be noticed in the form of a gap between observed transit times and the hypothetical constant speed curves. We also note that mean ICME speeds (considering all the events plotted in panels **a** and **b**) for Solar Cycle 23 (508 km s^{-1}) are significantly higher than those for Cycle 24 (443 km s^{-1}), which implies low-speed dominated solar wind conditions during Cycle 24.

constant speed which is equal to ICME speed at 1 AU. We notice that most of the CMEs lie below the hypothetical transit-time curve for constant speed which readily suggests that the majority of CMEs traveled faster than their final speeds at 1 AU. There are only a few events that lie on or above the dashed curve, indicating the possibility of intermittent phases of acceleration of these CMEs in the interplanetary medium. However, such events occur in the lower speed range only (*i.e.* ICME speed $< 500\ \mathrm{km\,s^{-1}}$). The mean ICME speed *versus* transit-time profiles also shows a distinct gap between high-speed ICMEs ($\gtrsim 500\ \mathrm{km\,s^{-1}}$) indicated with dashed curves. In fact, at this speed range, none of the events lie close to the dashed line. This feature can be seen for both MC and EJ type events (Figures 10(c) and (f)).

3.4. CME–ICME Speed Relations

In Figure 11, we plot the mean ICME speed at the near-Earth region as a function of the initial CME speed for all ICME events (top panels) as well as MC and EJ events separately (middle and bottom panels, respectively). The plot comprising all ICME cases suggests a general trend in which the ICME speed increases with initial CME speed. The dotted line in Figure 11a and b indicates a constant velocity line (*i.e.* it implies a hypothetical situation in which CMEs neither accelerate nor decelerate). The best fit curves corresponding to the quadratic fitting intersect the constant speed line at $\approx 400\ \mathrm{km\,s^{-1}}$ for both cycles, which is nearly equal to the ambient solar wind speed. This intersection value approximately indicates the speed above which the deceleration of a CME is effective.

When we consider the CME–ICME speed relation for the MC and EJ cases separately for the two cycles, we find an interesting scenario (middle and bottom panels of Figure 11). The curves of the second order best fitting during Cycle 23 for both MC and EJ type events indicate a gradual rise in ICME speed at 1 AU with initial CME speed. On the other hand, ICME–CME speed relations for Cycle 24 for both MC and EJ events exhibit rising and decreasing trends for lower and higher CME speeds, respectively.

3.5. Interplanetary Acceleration of CMEs

In Figure 12, we present the effective acceleration that ICMEs experience as they travel in the interplanetary medium as a function of the initial speed of CMEs. Here the IP acceleration of a CME is the ratio between the difference in the initial and final speeds of the CME and the transit time of the ICME. The final speed of the CME is essentially the ICME speed measured at 1 AU. We have studied the relation between IP acceleration and initial CME speed for all ICME, MC, and EJ type events and the corresponding plots are shown in the top, middle and bottom panels of Figure 12. These plots clearly indicate that most CMEs are decelerated in the interplanetary medium except for very low-speed CMEs with initial speed less than $\approx 450\ \mathrm{km\,s^{-1}}$. It is also evident that with the increase in CME initial speed, the net deceleration gradually increases. The IP accelerations *versus* CME initial speed profiles separately for MC and EJ events are consistent with the general trend seen in the total ICME population. One can also notice that CMEs decelerate faster with CME initial speed for Cycle 23 than for Cycle 24. To illustrate the CME acceleration associated differences between Cycles 23 and 24, we have plotted a horizontal dotted line at an arbitrary acceleration value of $-5\ \mathrm{m\,s^{-2}}$. We see that, in all cases, the dotted line intersects with the best fitted curve at lower initial CME speed (indicated by arrows) for Cycle 23 ($\approx 1500\ \mathrm{km\,s^{-1}}$) compared with the next cycle ($\approx 1600\ \mathrm{km\,s^{-1}}$). This difference also reflects the fact that Cycle 24 has a significantly smaller number of high-speed events (which are subject to higher deceleration) than Cycle 23, which has a restricted number of data points for polynomial fittings at higher speeds. However, within a given cycle the profiles of IP acceleration and CME initial speed remain similar for the MC and the EJ cases.

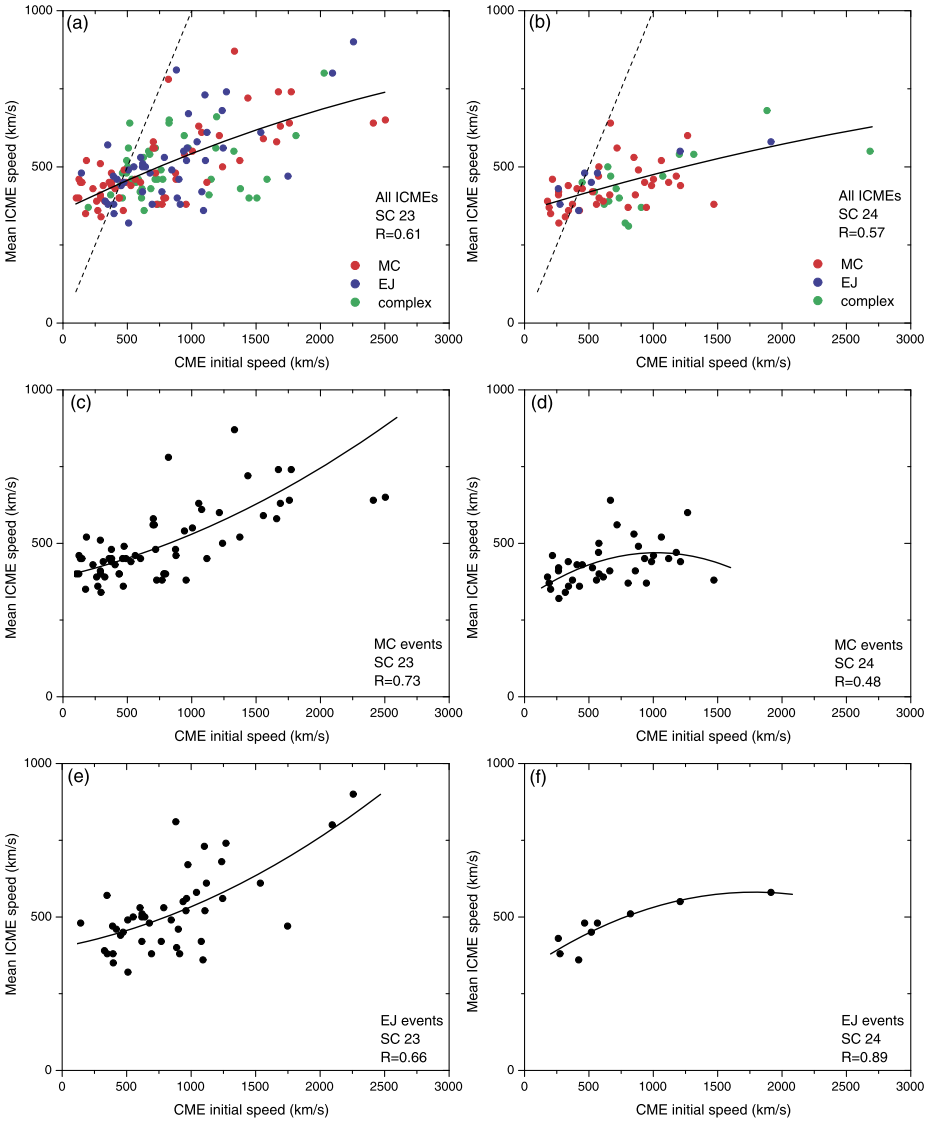

Figure 11 Relations between the initial CME speeds and the ICME speeds at 1 AU for Solar Cycles 23 (*left panels*) and 24 (*right panels*), for all ICMEs (*top panels*), MC (middle panels) and EJ type events (*bottom panels*). The *black curves* indicate the quadratic least-squares fit to the data points. The correlation coefficient (R) for the quadratic fitting is shown at the *top right corner of each panel*. The *dashed lines* in the *top panels* indicate the assumed constant velocity profiles for CMEs.

4. Summary and Discussions

In this article, we carry out a statistical study of ICMEs to understand their propagation characteristics and consequences at 1 AU during Solar Cycles 23 and 24. In order to better understand the CME–ICME relation, we further consider two subsets of ICMEs, MCs and EJs, separately. Our work is based on a simple analysis, but it presents an overview

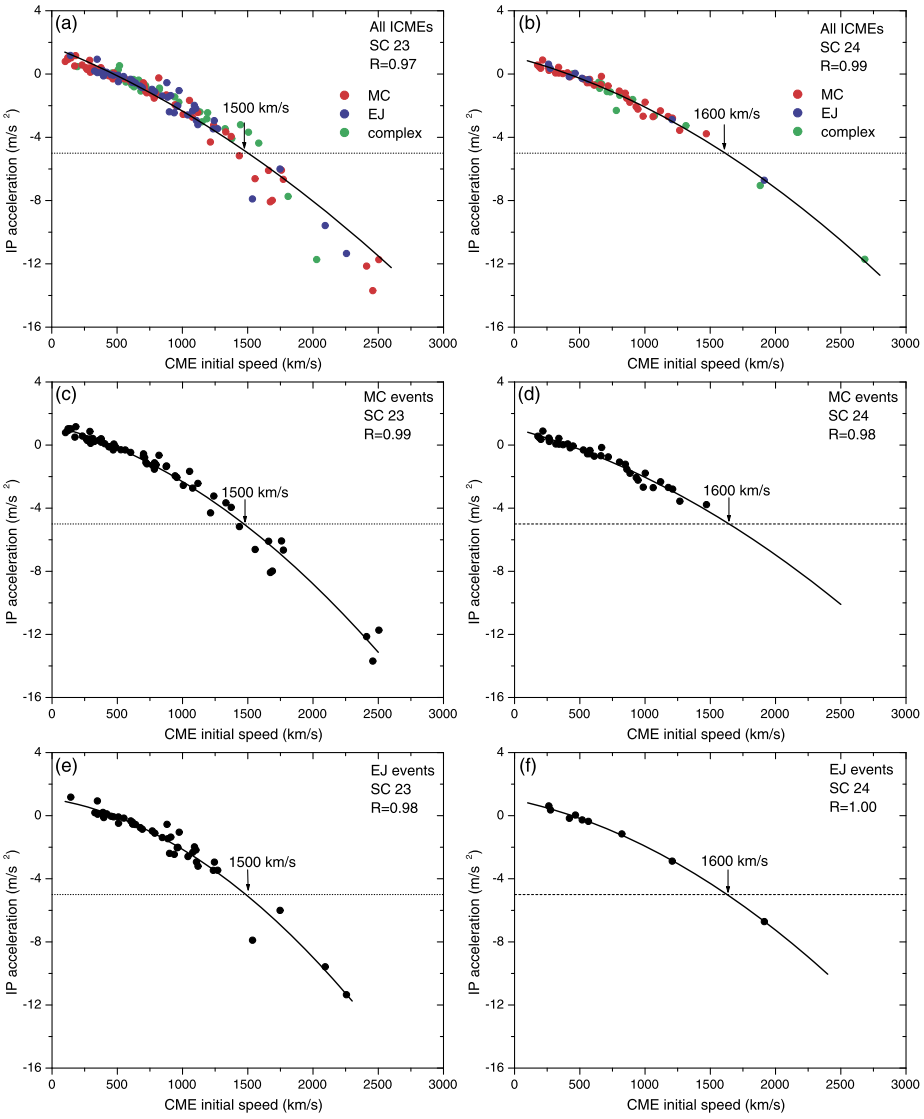

Figure 12 Relation between the initial CME speeds and the IP accelerations for all ICMEs (*top panels*), MC (*middle panels*) and EJ type events (*bottom panels*). *Left and right panels* indicate plots for Solar Cycles 23 and 24, respectively. The *black curves* indicate the quadratic least-squares fit to the data points. The correlation coefficient (R) for the quadratic fitting is shown at the *top right corner of each panel*. To illustrate the relation of IP accelerations as a function of CME initial speeds during Solar Cycles 23 and 24, we have drawn a *dotted horizontal line* at an arbitrary acceleration value of $-5\ \mathrm{m\,s^{-2}}$. We note that the *dotted line* intersects with the best fitted curve at lower initial speed for Cycle 23 ($\approx 1500\ \mathrm{km\,s^{-1}}$) compared to the next solar cycle ($\approx 1600\ \mathrm{km\,s^{-1}}$), which means that, for Cycle 24, ICME decelerations increase slowly with the increase of CME initial speeds. However, within a given cycle the profiles of IP accelerations and CME initial speeds remain similar for the MC and EJ cases.

and comparison of the propagation characteristics of the ICMEs during two complete solar cycles.

Our study reveals that Solar Cycle 24 shows a significant reduction in the number of ICME events compared with the previous cycle (Figure 5). The drastic reduction of ICME activity during Solar Cycle 24 can be seen in the light of its weak magnetic activity in comparison with Cycle 23, as evidenced by sunspot observations (Figure 5c), which has eventually resulted in much fewer CMEs and subsequent ICMEs. Notably, the fraction of MC type events is much larger during Cycle 24 (60%) than during Cycle 23 (41%). In this context, we note that, despite a larger number of MCs, the geoeffectiveness in Solar Cycle 24 is very low (Gopalswamy *et al.*, 2015). Furthermore, interplanetary scintillation (IPS) observations suggest a low-speed dominated background solar wind conditions during Cycle 24 (Manoharan *et al.*, 2016; Johri and Manoharan, 2016). The comparison between histograms of initial speed of CMEs and 1 AU speed of ICMEs indicates a narrower range in the speed of ICMEs compared with their near-Sun counterparts. This finding is consistent with the general understanding that CMEs effectively slow down during their propagation in the interplanetary medium because of their interaction with the background solar wind (Vršnak *et al.*, 2013; Shanmugaraju and Vršnak, 2014; Syed Ibrahim, Manoharan, and Shanmugaraju, 2017).

As expected, there is a general trend of decrease in ICME transit-times with respect to initial CME speeds (Figures 6 and 8). However, there is a broad range in transit times of ICMEs for a given initial CME speed, which suggests that each CME has a different propagation profile. These results are consistent with earlier works (see, *e.g.*, Michałek *et al.*, 2004; Manoharan *et al.*, 2004; Manoharan, 2006; Syed Ibrahim, Shanmugaraju, and Bendict Lawrance, 2015). We also note that almost all ICMEs travel in the interplanetary medium faster than with their final speeds (Figure 10), which implies that every event is subject to the aerodynamical drag force in the background solar wind, which tends to equalize the speed of the CME to that of the solar wind (see, *e.g.*, Gopalswamy *et al.*, 2001; Manoharan, 2006). Our analysis clearly indicates that (see Figure 10) the transit time for fast ICMEs ($\gtrsim 500$ km s^{-1}) is shorter than expected from their observed speeds at 1 AU, which can be noticed in the form of a horizontal gap between the observed transit times and the hypothetical constant speed curve. This interesting feature implies that high-speed ICMEs acquire a much higher internal energy from the source active regions during the initiation process, which effectively overcomes the aerodynamic drag force, while the CMEs transit the interplanetary medium (Manoharan, 2010). In this context, it is noteworthy that Solar Cycle 24 significantly lacks high-speed CMEs in comparison with the previous cycle (*cf.* Figures 3a and b). This means that under the conditions of low-speed dominated solar wind and a minority of high-speed CME events during Cycle 24, the drag applied by the background solar wind to the CME propagation (which is proportional to $|V_{\rm CME} - V_{\rm Solar\ Wind}|$) will, on the whole, be less effective.

In general, the mean ICME speed increases with an increase in the initial CME speed (Figure 11). Also we note that, for a given initial speed, the ICME arrival speed at 1 AU exhibits a wide range. However, the relationships between CME initial and final (*i.e.* 1 AU) speeds for Cycles 23 and 24, as represented by the second order polynomial, show different trends when viewed separately for MC and EJ events (*cf.* Figures 11c – f). Such differences imply that a combination of multiple parameters affect the evolution of ICMEs, such as CME properties at the near-Sun region (*e.g.* speed, acceleration, and structure) along with changes in the background solar wind. Irrespective of this, the similarities in the general trends of the ICME–CME speed relations for MC and EJ within the same cycle are also noteworthy (*cf.* Figures 11c – f). The CME propagation from the Sun to the near-Earth environment shows an overall positive as well as negative acceleration (*i.e.* deceleration), although the acceleration is limited to only low-speed CMEs that are launched with speeds comparable with or

less than that of the mean solar wind speed, *i.e.* $\approx 400-450$ km s^{-1} (Figure 12). Notably, the effective deceleration increases with the initial speed of the CME. These results imply that, for slow CMEs (< 400 km s^{-1}), the energy is transferred from the solar wind to the CMEs, while faster events ($\gtrsim 400$ km s^{-1}) tend to lose their energy to the ambient medium. Within a given cycle, the similarities of MC and EJ profiles with respect to CME–ICME speed relations as well as IP accelerations suggest that the underlying physical structure that supports the propagation of both kinds of ICMEs through the interplanetary medium is the same. These observations are consistent with the assumption that all CMEs have a flux rope structure and that the trajectory of the CMEs essentially determines the observed ICME structure at 1 AU (Marubashi, 2000; Kim *et al.*, 2013; Marubashi *et al.*, 2015)

Acknowledgements We gratefully acknowledge the catalog of "Near-Sun Interplanetary Coronal Mass Ejections Since January 1996" compiled by Ian Richardson and Hilary Cane, which is the basis for the present study. The basic CME parameters were taken from the LASCO CME catalog. This CME catalog is generated and maintained at the CDAW Data Center by NASA and The Catholic University of America in cooperation with the Naval Research Laboratory. SOHO is a project of international cooperation between ESA and NASA. K.S.C and R.S.K acknowledge support from KASI basic research fund and the R&D program "Development of a Solar Coronagraph on the International Space Station (Project No. 2019-1-850-02) supervised by the Ministry of Science and ICT". We sincerely thank the anonymous referee for providing constructive comments and suggestions, which have significantly enhanced the presentation and quality of the paper.

Disclosure of Potential Conflict of Interest The authors declare that they have no conflict of interest.

Publisher's Note Springer Nature remains neutral with regard to jurisdictional claims in published maps and institutional affiliations.

References

Burlaga, L.: 2001, Terminology of ejecta in solar wind. *Eos Trans. AGU* **82**, 433.

Burlaga, L., Sittler, E., Mariani, F., Schwenn, R.: 1981, Magnetic loop behind an interplanetary shock – Voyager, Helios, and IMP 8 observations. *J. Geophys. Res.* **86**, 6673. DOI. ADS.

Burlaga, L.F., Skoug, R.M., Smith, C.W., Webb, D.F., Zurbuchen, T.H., Reinard, A.: 2001, Fast ejecta during the ascending phase of solar cycle 23: ACE observations, 1998 – 1999. *J. Geophys. Res.* **106**, 20957. DOI. ADS.

Cane, H.V., Richardson, I.G.: 2003, Interplanetary coronal mass ejections in the near-Earth solar wind during 1996 – 2002. *J. Geophys. Res.* **108**, 1156. DOI. ADS.

Chen, J.: 2017, Physics of erupting solar flux ropes: Coronal mass ejections (CMEs) – Recent advances in theory and observation. *Phys. Plasmas* **24**(9), 090501. DOI. ADS.

Cho, K.-S., Park, S.-H., Marubashi, K., Gopalswamy, N., Akiyama, S., Yashiro, S., Kim, R.-S., Lim, E.-K.: 2013, Comparison of helicity signs in interplanetary CMEs and their solar source regions. *Solar Phys.* **284**, 105. DOI. ADS.

Dere, K.P., Brueckner, G.E., Howard, R.A., Michels, D.J., Delaboudiniere, J.P.: 1999, LASCO and EIT observations of helical structure in coronal mass ejections. *Astrophys. J.* **516**, 465. DOI. ADS.

Gopalswamy, N., Lara, A., Yashiro, S., Kaiser, M.L., Howard, R.A.: 2001, Predicting the 1-AU arrival times of coronal mass ejections. *J. Geophys. Res.* **106**, 29207. DOI. ADS.

Gopalswamy, N., Yashiro, S., Xie, H., Akiyama, S., Mäkelä, P.: 2015, Properties and geoeffectiveness of magnetic clouds during solar cycles 23 and 24. *J. Geophys. Res.* **120**, 9221. DOI. ADS.

Gosling, J.T.: 1990, *Coronal Mass Ejections and Magnetic Flux Ropes in Interplanetary Space*, *AGU Geophys. Monograph Ser.* **58**, 343. DOI. ADS.

Johri, A., Manoharan, P.K.: 2016, An intense flare-CME event in 2015: Propagation and interaction effects between the Sun and Earth's orbit. *Solar Phys.* **291**, 1433. DOI. ADS.

Kim, R.-S., Gopalswamy, N., Cho, K.-S., Moon, Y.-J., Yashiro, S.: 2013, Propagation characteristics of CMEs associated with magnetic clouds and ejecta. *Solar Phys.* **284**, 77. DOI. ADS.

Klein, L.W., Burlaga, L.F.: 1982, Interplanetary magnetic clouds at 1 AU. *J. Geophys. Res.* **87**, 613. DOI. ADS.

Manoharan, P.K.: 2006, Evolution of coronal mass ejections in the inner heliosphere: A study using white-light and scintillation images. *Solar Phys.* **235**, 345. DOI. ADS.

Manoharan, P.K.: 2010, Ooty interplanetary scintillation – Remote-sensing observations and analysis of coronal mass ejections in the heliosphere. *Solar Phys.* **265**, 137. DOI. ADS.

Manoharan, P.K., Gopalswamy, N., Yashiro, S., Lara, A., Michalek, G., Howard, R.A.: 2004, Influence of coronal mass ejection interaction on propagation of interplanetary shocks. *J. Geophys. Res.* **109**, A06109. DOI. ADS.

Manoharan, P.K., Maia, D., Johri, A., Induja, M.S.: 2016, Interplanetary consequences of coronal mass ejection events occurred during 18 – 25 June 2015. In: Dorotovic, I., Fischer, C.E., Temmer, M. (eds.) *Coimbra Solar Physics Meeting: Ground-Based Solar Observations in the Space Instrumentation Era*, *Astron. Soc. Pacific Conf. Ser.* **504**, 59. ADS.

Marubashi, K.: 2000, Physics of interplanetary magnetic flux ropes: Toward prediction of geomagnetic storms. *Adv. Space Res.* **26**, 55. DOI. ADS.

Marubashi, K., Akiyama, S., Yashiro, S., Gopalswamy, N., Cho, K.-S., Park, Y.-D.: 2015, Geometrical relationship between interplanetary flux ropes and their solar sources. *Solar Phys.* **290**, 1371. DOI. ADS.

Michałek, G., Gopalswamy, N., Lara, A., Manoharan, P.K.: 2004, Arrival time of halo coronal mass ejections in the vicinity of the Earth. *Astron. Astrophys.* **423**, 729. DOI. ADS.

Richardson, I.G., Cane, H.V.: 2004, Identification of interplanetary coronal mass ejections at 1 AU using multiple solar wind plasma composition anomalies. *J. Geophys. Res.* **109**, A09104. DOI. ADS.

Schmieder, B., Aulanier, G., Vršnak, B.: 2015, Flare-CME models: An observational perspective (invited review). *Solar Phys.* **290**, 3457. DOI. ADS.

Shanmugaraju, A., Vršnak, B.: 2014, Transit time of coronal mass ejections under different ambient solar wind conditions. *Solar Phys.* **289**, 339. DOI. ADS.

Syed Ibrahim, M., Manoharan, P.K., Shanmugaraju, A.: 2017, Propagation of coronal mass ejections observed during the rising phase of solar cycle 24. *Solar Phys.* **292**, 133. DOI. ADS.

Syed Ibrahim, M., Shanmugaraju, A., Bendict Lawrance, M.: 2015, Transit time of CME/shock associated with four major geo-effective CMEs in solar cycle 24. *Adv. Space Res.* **55**, 407. DOI. ADS.

Vršnak, B., Žic, T., Vrbanec, D., Temmer, M., Rollett, T., Möstl, C., Veronig, A., Čalogović, J., Dumbović, M., Lulić, S., Moon, Y.-J., Shanmugaraju, A.: 2013, Propagation of interplanetary coronal mass ejections: The drag-based model. *Solar Phys.* **285**, 295. DOI. ADS.

Webb, D.F., Howard, T.A.: 2012, Coronal mass ejections: Observations. *Living Rev. Solar Phys.* **9**, 3. DOI. ADS.

Xie, H., Gopalswamy, N., St. Cyr, O.C.: 2013, Near-Sun flux-rope structure of CMEs. *Solar Phys.* **284**, 47. DOI. ADS.

Zurbuchen, T.H., Richardson, I.G.: 2006, In-situ solar wind and magnetic field signatures of interplanetary coronal mass ejections. *Space Sci. Rev.* **123**, 31. DOI. ADS.